Hot gas around SN 1998bw - Inferring the progenitor from its environment[*]

T. Krühler[1], H. Kuncarayakti[2, 3, 4, 5], P. Schady[1], J. P. Anderson[6], L. Galbany[7], and J. Gensior[8]

[1] Max-Planck-Institut für extraterrestrische Physik, Giessenbachstraße, 85748 Garching, Germany

[2] Finnish Centre for Astronomy with ESO (FINCA), University of Turku, Väisäläntie 20, 21500 Piikkiö, Finland

[3] Tuorla Observatory, Department of Physics and Astronomy, University of Turku, Väisäläntie 20, 21500 Piikkiö, Finland

[4] Millennium Institute of Astrophysics, Casilla 36-D, Santiago, Chile

[5] Departamento de Astronomía, Universidad de Chile, Casilla 36-D, Santiago, Chile

[6] European Southern Observatory, Alonso de Córdova 3107, Vitacura, Casilla 19001, Santiago 19, Chile

[7] PITT PACC, Department of Physics and Astronomy, University of Pittsburgh, Pittsburgh, PA 15260, USA

[8] School of Physics and Astronomy, University of Edinburgh, Peter Guthrie Tait Road, Edinburgh EH9 3FD, UK

March 23, 2017

ABSTRACT

Spatially-resolved spectroscopy of the environments of explosive transients carries detailed information about the physical properties of the stellar population that gave rise to the explosion, and thus the progenitor itself. Here, we present new observations of ESO184-G82, the galaxy hosting the archetype of the γ-ray burst/supernova connection, GRB 980425/SN 1998bw, obtained with the integral-field spectrograph MUSE at the VLT. These observations yield detailed maps of emission-line strength for various nebular lines, as well as physical parameters like dust extinction, stellar age, and oxygen abundance on spatial scales of 160 pc. The immediate environment of GRB 980425 is young $(5 - 8 \, \mathrm{Myr})$ and consistent with a mildly-extinguished $(A_V \sim 0.1 \, \mathrm{mag})$ progenitor of zero-age main-sequence mass between $25 \, \mathrm{M_\odot}$ and $40 \, \mathrm{M_\odot}$ and oxygen abundance $12 + \log(\mathrm{O/H}) \sim 8.2$ $(Z \sim 0.3 \, \mathrm{Z_\odot})$, slightly lower than the one of an integrated measurement of the whole galaxy $(12+\log(\mathrm{O/H}) \sim 8.3)$ and a prominent nearby H ɪɪ-region $(12+\log(\mathrm{O/H}) \sim 8.4)$.

This region is significantly younger than the explosion site, and we argue that a scenario in which the GRB progenitor formed there and was subsequently ejected appears very unlikely. We show that empirical strong-line methods based on [O III] and/or [N II] are inadequate to produce accurate maps of oxygen abundance at the level of detail of our MUSE observation as these methods strongly depend on the ionization state of the gas. The metallicity gradient in ESO184-G82 is -0.06 dex kpc^{-1}, indicating that the typical offsets of at most few kpc for cosmological GRBs have a small impact for oxygen-abundance measurements at higher redshift on average. Similarly, the spectrum from the GRB/SN site returns physical parameters that are broadly comparable **to** those inferred from an galaxy-integrated spectrum.

Key words. Gamma-ray burst: general, individual: GRB 980425, Galaxies: ISM, star formation, abundances

1. Introduction

Line emission from recombination of ionized hydrogen, or from the decay of collisionally-excited states of metal ions **is a fundamental tracer of the physical conditions in H II regions**. The absolute and relative intensities of these transitions crucially depend on the ionizing source, the electron density in the plasma, the ionization state of the elements, and gas-phase abundances (Osterbrock 1989). This makes emission-line spectra of astronomical sources one of the most elementary diagnostics of galaxy formation and evolution (e.g. Tremonti et al. 2004; Erb et al. 2006; Förster Schreiber et al. 2009). The total intensity of the hydrogen recombination lines, for example, is proportional the number of O-type stars, and thus traces the star-formation rate at timescales of $\sim 10\,\mathrm{Myr}$ (e.g. Kennicutt 1998). The continuum emission at the wavelength of Hα in turn originates from B- or A-type stars, which makes the Hα equivalent width (EW) a good tracer of the age of the stellar population.

Metal abundances have been measured through ratios of prominent emission lines from ions such as O$^+$, O^{2+}, N$^+$, S$^+$ and/or recombination lines of hydrogen (Pagel et al. 1979; Alloin et al. 1979). Given their fundamental importance in galaxy evolution and cosmology, these abundance determinations through nebular emission lines have been the focus of a large body of literature (e.g. Kobulnicky & Kewley 2004; Pilyugin & Thuan 2005; Stasińska 2006; Izotov et al. 2006; Kewley & Ellison 2008).

It is thus immediately clear that an emission-line spectrum of cosmological sources carries detailed information about the underlying stellar population and thus has been used to infer properties not only of galaxies but also of the progenitors of explosive transients. Global (e.g. Prieto et al. 2008; Li et al. 2011) or local (e.g. Anderson et al. 2010; Modjaz et al. 2011; Leloudas et al. 2011) properties of nearby supernova hosts, as well as cosmological γ-ray bursts (GRBs, e.g. Wiersema et al. 2007; Krühler et al. 2012a; Graham & Fruchter 2013) or super-luminous supernovae (e.g.
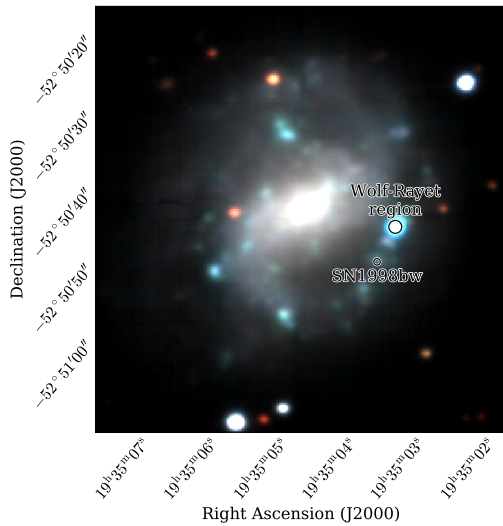
Fig. 1: False-color composite from reconstructed *VRI*-band images from the MUSE data cube. The image spans approximately 55" by 55", or 10 by 10 kpc. One MUSE spaxel corresponds to 35 pc. The effective spatial resolution is given by the point spread function with a FWHM of approximately 0.″9 or 160 pc.

Chen et al. 2013; Lunnan et al. 2014; Leloudas et al. 2015; Perley et al. 2016) have likewise been used to compare progenitor models with the expected environments.

A fundamental assumption of all these studies is the hypothesis that there is a tight relation between the primary observables of gas-phase oxygen abundance or age of H ɪɪ regions and metallicity or life time and thus initial mass of the progenitor star. Clearly, this link is most robust when coming from an analysis of the co-spatial stellar population. Integral-field spectroscopy (IFS) with high angular resolution is thus arguably the most comprehensive way of studying the environments of explosive transients. Low-redshift galaxies hosting supernovae (SNe), for example, are hence ideal targets for state-of-the-art integral-field units (IFUs, e.g. Kuncarayakti et al. 2013a,b; Galbany et al. 2014).

In contrast to SNe, the vast cosmological distances of GRBs (e.g. Fynbo et al. 2009; Tanvir et al. 2009; Krühler et al. 2012b) have always posed serious limitations on using IFS for GRB-selected galaxies. Only a few GRBs are close enough such that the spatial resolution achievable with modern ground-based instrumentation yields constraints on spatial scales better than a kpc. Spatially-resolved spectroscopy has therefore only been obtained for a handful of nearby GRB hosts using long-slit spectroscopy (e.g. Thöne et al. 2008; Levesque et al. 2011; Schady et al. 2015) or the previous generation of IFUs (Christensen et al. 2008; Thöne et al. 2014).

The focus of this article are our new observations of the poster-child of the GRB/SN connection, GRB 980425/SN 1998bw using the Multi-Unit Spectroscopic Explorer (MUSE, Bacon et al. 2010). GRB 980425 is the closest GRB yet discovered and both the GRB (e.g. Galama et al. 1998; Kulkarni et al. 1998), the SN (e.g. Iwamoto et al. 1998; Patat et al. 2001; Maeda et al. 2006) and host galaxy (e.g. Fynbo et al. 2000; Sollerman et al. 2005; Hammer et al. 2006; Michałowski et al. 2009, 2014, 2016; Le Floc'h et al. 2012; Arabsalmani et al. 2015) are extensively discussed in existing literature.

Compared to the bulk of cosmological GRBs, GRB 980425 is rather peculiar: the isotropic-equivalent release in γ-rays of GRB 980425 was $\sim 10^{48}$ erg (Galama et al. 1998), a factor of ten lower than other local, low-luminosity GRBs, or around five orders of magnitudes less than conventional, higher-redshift GRBs (Xu et al. 2013). No bright multi-wavelength afterglow was observed for GRB 980425 despite its proximity. However, the associated SN without hydrogen or helium in its spectrum, broad metal absorption lines and high luminosity has proven to be typical of GRB/SNe in general (Hjorth & Bloom 2012).

The host galaxy of GRB 980425/SN 1998bw, ESO184-G82 (Lauberts & Valentijn 1989), is a barred spiral dwarf galaxy (Fynbo et al. 2000) seen nearly face on (Fig. 1) with a visible **extent** of approximately 67" by 57" (12 x 10 kpc) at the $B = 26.5$ mag isophote (Sollerman et al. 2005). Its brightness, luminosity, and stellar mass are $B = 14.94$ mag, $M_B = -17.65$ mag or $L = 0.05\,\mathrm{L}^\star$, and $\log(M_*/\mathrm{M}_\odot) = 8.7$, respectively (Sollerman et al. 2005; Michałowski et al. 2014). SN 1998bw exploded in an H II-region 12" distant (2 kpc projected) from its center, and 860 pc to the South-East of a young star-forming region that displays signatures of Wolf-Rayet (WR) stars in its spectrum (Hammer et al. 2006), the so-called Wolf-Rayet region (Fig. 1).

Despite the large set of recent literature on GRB 980425/SN 1998bw and its host mentioned above, we summarize our new data and conclusions here mainly because of three reasons: the unique combination of spatial resolution and sensitivity of MUSE yields detailed maps of emission-line strength, dust reddening and oxygen abundance, which help us to clarify some of the ambiguities around SN 1998bw and its host from previous works. These maps provide the tightest and most accurate constraints on the immediate environment and underlying stellar population of SN 1998bw yet available and thus allow us to infer the GRB's progenitor properties from its parent stellar population. And last, they offer an informative example of spatially-resolved oxygen-abundance measurements in star-forming galaxies through strong line diagnostics and their dependence on other physical conditions in the interstellar medium (ISM).

Throughout the paper, we adopt a flat ΛCDM cosmology with Planck parameters ($H_0 = 67.3\,\mathrm{km\,s^{-1}\,Mpc^{-1}}$, Ω_m=0.315, Ω_Λ=0.685, Planck Collaboration 2014), a Chabrier (2003) initial mass function (IMF), solar abundances from Asplund et al. (2009), and report errors at the 1 σ confidence level.

2. Observations

We observed ESO184-G82 ($z = 0.0086$, or $D_L = 37$ Mpc) using the Multi-Unit Spectroscopic Explorer (MUSE, Bacon et al. 2010) at ESO's Very Large Telescope (VLT) during the two clear nights starting on 2015-05-14 and 2015-05-15 in a classical observing run from Paranal. In each night, we obtained four dithered exposures of 450 s integration each, totaling 3600 s on source. The on-target frames were supplemented by an offset pointing to blank sky for 200 s. For absolute flux calibration, the spectro-photometric standard LTT3218 was observed at the beginning of each

night. The full-width half maximum of the stellar point spread function, which defines our spatial resolution, is between 0″9 (at 9000 Å) and 1″1 (at 5000 Å) in the MUSE data.

MUSE is a state-of-the-art integral-field spectrograph, splitting the light into 24 identical sub-units. In the wide-field mode, each of these sub-IFUs disperses a 60" × 2.5" patch of the sky onto a single CCD. In this way, MUSE covers a continuous sky region of 60"×60" in the wavelength range between 4750 Å and 9300 Å when operated in its nominal configuration. With its excellent total throughput, small spaxel size (0″2×0″2), and decent resolving power ($1800 < R < 3600$ increasing from blue to red wavelengths), MUSE offers an unprecedented combination of sensitivity, spatial resolution and field of view for IFUs (Bacon et al. 2010).

3. Data Reduction

We reduced our MUSE data with the pipeline supplied through ESO[1] in its version `1.2.1` (Weilbacher et al. 2014), which applies corrections for bias level, flat-fields, illumination level and geometric distortions. The pipeline also performs the wavelength calibration using day-time arc-lamp frames, which is subsequently refined by sky-lines in the science data. The sky background was subtracted using the offset pointing through algorithms from the Zurich Atmospheric Package (Soto et al. 2016). The exposures from the two different nights were then corrected for slight pointing offsets between night one and two, stacked using variance-weighting, and de-reddened based on the Galactic foreground E_{B-V} = 0.05 mag (Schlafly & Finkbeiner 2011) assuming an average Milky-Way extinction law (Pei 1992) and R_V = 3.08.

We use the spectrum of the star at RA(J2000) = $19^h35^m02^s.00$**, Decl(J2000) = $-52°50′21″1$ to correct for telluric absorption via `molecfit` (Smette et al. 2015). By fitting the three prominent telluric absorption bands within the MUSE wavelength coverage (centered around 6870 Å, 7600 Å, and 7630 Å) with a physical model of the atmospheric molecular oxygen and water vapor content, we derive the telluric absorption for the single star, which we then subsequently apply to all spaxels.**

The final data cube has slight astrometric offsets, which we correct by tying the position of stars in the field of MUSE to coordinates from a reference image taken with the SOFI imager on NTT on 2000-10-25. We then measure the position of the SN in the reference frame, mapping it onto the MUSE cube with an accuracy of around 50 mas. Figure 1 shows a false-color image reconstructed from the MUSE cube where the position of SN 1998bw is indicated.

Similarly, we use photometry to corroborate our flux calibration through the V, R_C and I_C-band magnitudes of star 1 of Clocchiatti et al. (2011) and synthetic photometry from the MUSE data cube, yielding differences of ΔV = 0.05 ± 0.03 mag, ΔR_C = 0.05 ± 0.06 mag and ΔI_X = 0.00 ± 0.05 mag. After applying a linear fit in wavelength to these correction terms, we can accurately reproduce the optical colors of the host galaxy (Sollerman et al. 2005) to better than 0.02 mag.

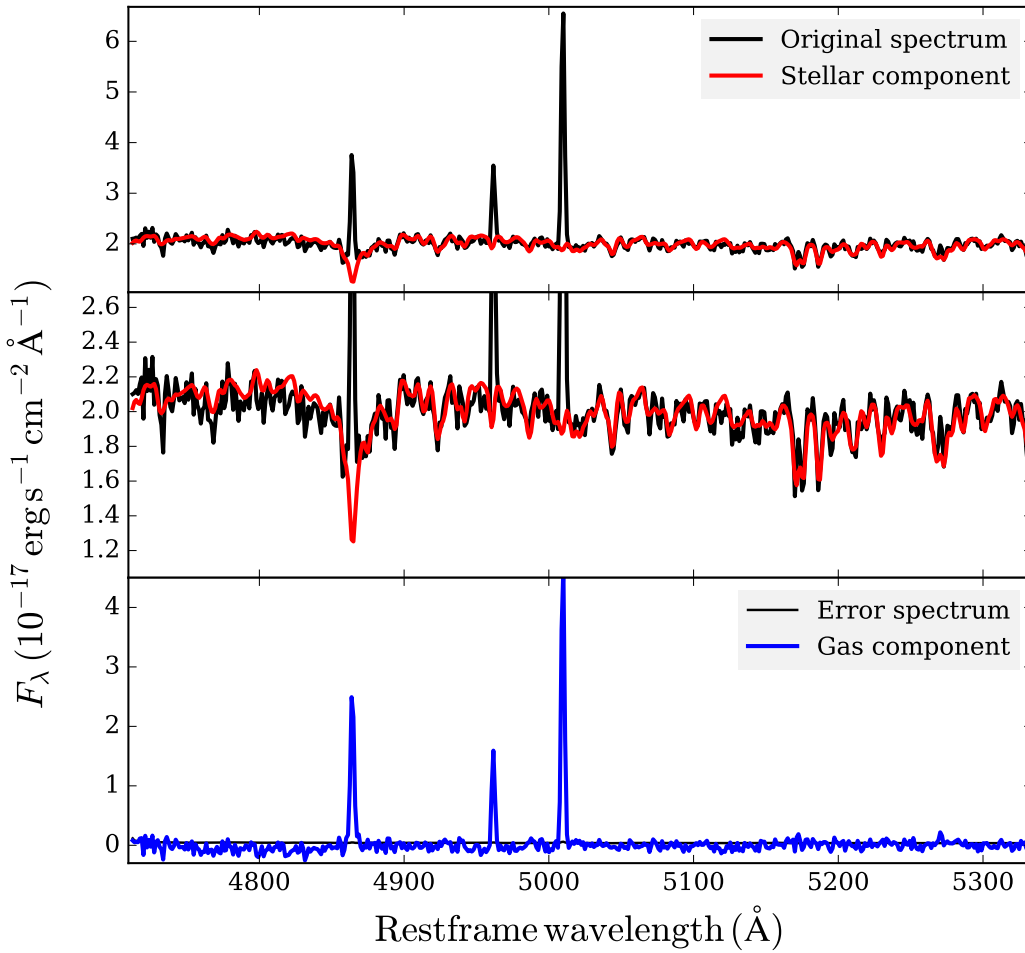[1]http://www.eso.org/sci/software/pipelines/

Fig. 2: Separating stellar and gas-phase spectra in the MUSE data cube. This figure shows the **rest-frame wavelength region around Hβ including the two strong [O III]($\lambda\lambda$4959, 5007) transitions at a random location in the MUSE cube. Black is the original spectrum, red the fitted stellar component (*upper* and *middle panel*). The *middle panel* shows a zoom-in to the continuum. In the *lowest panel*, the resulting spectrum of the gas-phase contribution is shown in blue, while the black line represents the error spectrum.** Note the significant Balmer absorption around Hβ.

4. Analysis and Discussion

4.1. Separating Gas-phase and Stellar Component.

As we are primarily interested in the absolute and relative strengths of the nebular lines, and thus the ionized gas component of the galaxy, we need to remove the stellar Balmer absorption for accurate line flux measurements, in particular for Hβ (Fig. 2). The strength of the stellar absorption is primarily a function of the age of the underlying stellar population. It thus depends on the position within a galaxy, and needs to be accurately modeled for reliable constraints on the Balmer decrement which we will use to measure dust reddening maps.

We separate the galaxy's star and gas components by fitting a linear superposition of template stellar spectra based on the Bruzual & Charlot (2003) models to the MUSE data. We divide the full field of view into regions with a size of $0\rlap{.}''4 \times 0\rlap{.}''4$ (or 2×2 spaxels), and extract spectra for each of the ~ 22000 sub-regions. These spectra are then fit with stellar population models using `starlight` (Cid Fernandes et al. 2005, 2009) in a similar fashion to what we have done elsewhere
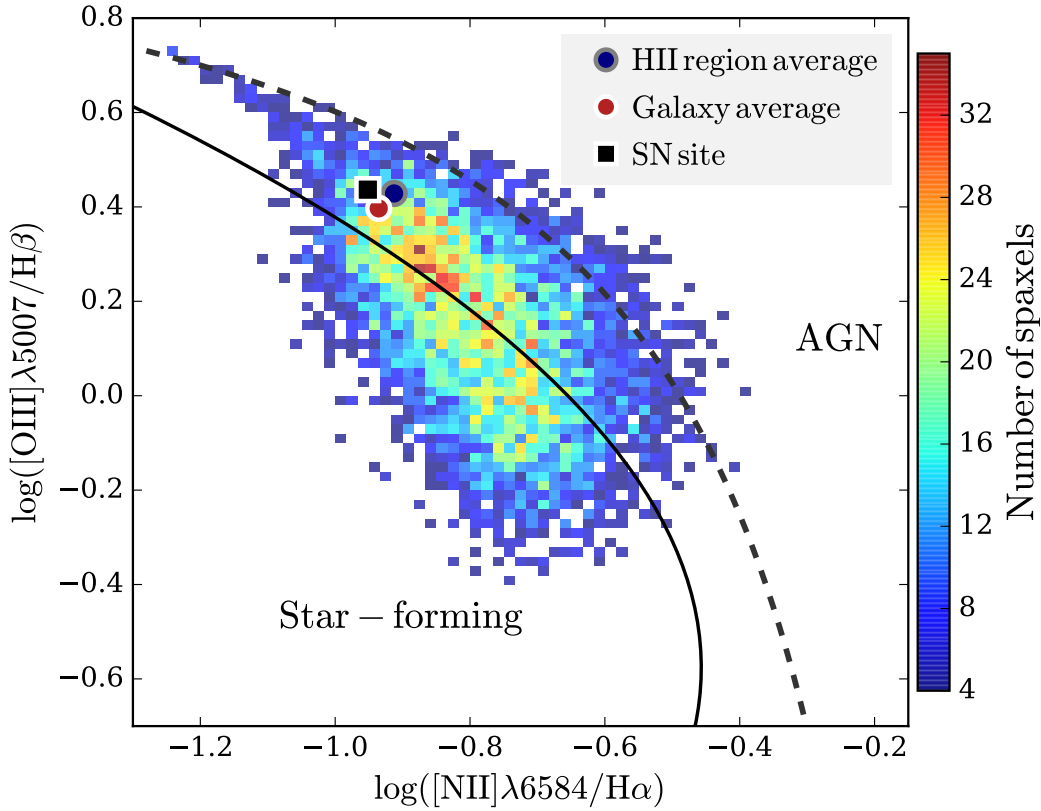
Fig. 3: Spaxel BPT diagram for ESO184-G82. The solid line denotes the ridge-line of SDSS galaxies (Brinchmann et al. 2008), whereas the dotted line represents the $z = 0$ classification line between star-formation and AGN as ionization source (Kewley et al. 2013). The GRB/SN explosion site, a galaxy average (including all spaxels) as well as an H II-region average (including only spaxels with $EW_{H\alpha} > 10\,\text{Å}$) are indicated.

for MUSE data (Galbany et al. 2016a; Kuncarayakti et al. 2016; Prieto et al. 2016). The 2×2 co-adding effectively increases the signal-to-noise ratio (SNR) at the expense of spatial resolution for the stellar properties, but is necessary to robustly perform an automated fit in particular in the fainter regions of the galaxy. We then linearly scale the best-fit stellar template to the intensity in single spaxels. Subtracting this stellar component from the original data leaves us with the spectral contribution of the gas-phase only (Fig. 2).

After having separated gas-phase and stellar component it is trivial to produce maps of line flux (integral over the gas-phase), continuum (average of the stellar component) and equivalent width (flux over continuum).

Plotting the characteristic emission-line flux ratios of [O III]/Hβ versus [N II]/Hα for individual spaxels in the BPT-diagram (Baldwin et al. 1981) allows us to immediately discard active galactic nuclei or shocks as the ionization source, and to confirm that young stars are the origin for the line-emission from ionized gas in ESO184-G82 (Fig. 3).
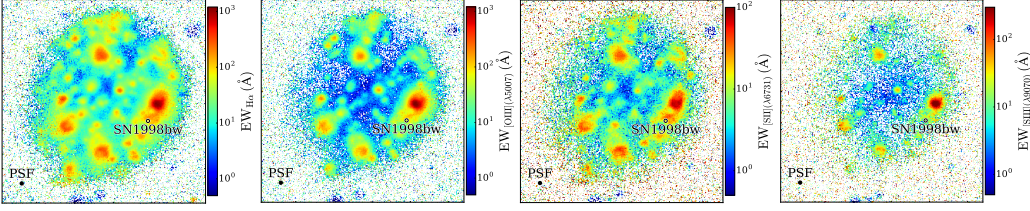
Fig. 4: Reconstructed images from the MUSE data cube. Each panel shows the host of GRB 980425 in a different nebular line. *Top-left*: Hα, *top-right*: [O III](λ5007), *bottom-left*: [S II](λ6731), *bottom-right*: [S III](λ9070). All panels are approximately 55" by 55", or 10 by 10 kpc in comoving size. One MUSE spaxel corresponds to 35 pc. The effective spatial resolution is given by the point spread function indicated in the lower left corner of each image with a FWHM of approximately 0.''9 or 160 pc.

4.2. Equivalent Width Maps and Stellar Population Ages

The Hα equivalent width map, which is a rather direct proxy of stellar population age, in particular for young stellar populations, is shown in Fig. 4. The spaxel closest to the SN/GRB position has an Hα equivalent width of $EW_{H\alpha} = 98 \pm 4$ Å. The spaxels within a radius of 70 pc yield $EW_{H\alpha} = 92 \pm 15$ Å.

Assuming a single stellar population from an instantaneous starburst, this $EW_{H\alpha}$ corresponds to stellar-population ages between 5 Myr and 8 Myr[2] from various models at metallicities of $Z = 0.2 Z_\odot$ (see e.g. Levesque & Leitherer 2013; Kuncarayakti et al. 2016, and references therein). The relatively large range in age is almost entirely due to the spread from different stellar evolution models or initial mass functions. These ages corresponds to life-times of stars with zero-age main sequence (ZAMS) masses between approximately 25 and 40 $M_\odot$ (Fagotto et al. 1994; Meynet & Maeder 2005). This is consistent with the SN's ejected oxygen mass ($M_O \sim 5-6 M_\odot$ evolved from a $M_{ZAMS} \sim 30 - 40 M_\odot$ star) derived through modeling the SN 1998bw nebular spectra (Mazzali et al. 2001; Maeda et al. 2006).

These considerations are only valid, of course, if the progenitor was born where it exploded, and was not ejected from the nearby WR region (Hammer et al. 2006). However, this region is so young that timing arguments make an ejection scenario quite contrived: Very high EW values of Hα and nebular transitions are observed in the center of the WR region ($EW_{H\alpha} > 900$ Å and $EW_{[O III](\lambda5007)} > 850$ Å)[3]. **Together with the detection of strong He I(λ4922) with an $EW_{HeI(\lambda4922)} = 3.5 \pm 0.2$ Å**, they ascertain population ages younger than 3 Myr (see also Appendix A) in instantaneous star-burst models, or $M_{ZAMS} \gtrsim 60 M_\odot$ (see e.g. Thöne et al. 2015, and references therein for a similar case). The discrepancy with respect to the progenitor mass from SN modeling (e.g., Mazzali et al. 2001; Maeda et al. 2006) then suggests that the GRB progenitor was indeed not born in the WR region, but rather formed in situ.

---

[2]**Constraints from other, age-sensitive lines like Hβ or He I (González Delgado et al. 1999) as well as the stellar continuum (Sect. A) generally agree with this age range.**

[3]These are strictly lower limits. The fact that the compact WR region is convolved with the seeing-introduced spatial scale of ~0.''9 leads to a smoothed EW distribution. In fact, archival VLT/FORS2 data discussed in the Appendix were taken under significantly better atmospheric conditions and show $EW_{[O III](\lambda5007)} \sim 2000$ Å (Appendix A).

For the progenitor to travel to the explosion site in less time than the age of the WR region ($< 3\,\mathrm{Myr}$), the peculiar velocities v would have to be extremely high ($v > 260\,\mathrm{km\,s^{-1}}$). This is again a strict lower limit, as projection effects further increase the required velocities. Scenarios that are believed to give rise to these kind of massive runaway stars are dynamical few-body encounters or binary supernovae, but both seem unfeasible here: A dynamical ejection produces hyper-velocity stars in only very rare and extreme cases (Hoogerwerf et al. 2001; Perets & Šubr 2012), and the probability of potential GRB progenitors ($M_{\mathrm{ZAMS}} \gtrsim 20\,M_\odot$) with velocity kicks of $> 200\,\mathrm{km\,s^{-1}}$ from a companion SN is also practically zero (Eldridge et al. 2011). This makes a binary supernova origin highly implausible as there simply would not be enough time to evolve and explode the primary and eject the secondary to a distance $\gtrsim 860\,\mathrm{pc}$. Also the fraction of stars ejected by dynamical encounters is of course a function of the elapsed time after star burst, and reaches only 0.01/0.03 at 1 Myr or 3 Myr at $M_{\mathrm{ZAMS}} \sim 35\,M_\odot$ (Banerjee et al. 2012), again leaving little time for the ejected star to travel as far as 860 pc (or further).

Given the presence of massive stars in the vicinity of the SN position (Fynbo et al. 2000), the substantial level of recent star-formation as evidenced through high EW of nebular lines at the SN position (Fig. 4), and the consistency between M_{ZAMS} derived from the age of the stellar population as well as the SN 1998bw nebular spectra, we see no compelling reason to invoke an artificial ejection from the nearby H ıı-region region to explain the GRB location within its host.

4.3. Dust Distribution

Due to its exquisite photometric and spectroscopic data coverage, SN 1998bw is widely used as a comparison object. Deriving its intrinsic properties like luminosity or color, however, requires an accurate knowledge of the absorbing dust column in its host, which we infer here through the Balmer lines. We convert line fluxes of Hα and Hβ into a map of color-excess E_{B-V} as shown in Fig. 5 using Eq. 5 of Krühler et al. (2015). This procedure assumes standard ratios of the Balmer lines at $10^4\,\mathrm{K}$ and $n_e \sim 100\,\mathrm{cm^{-3}}$ from Osterbrock (1989), broadly consistent with the values obtained for this galaxy (Table 1). Our results depend only marginally on our choice of an average Milky-Way extinction law (Pei 1992) with $R_V = 3.08$, as the difference between reddening laws in the local group is small in the wavelength range probed by Hα and Hβ.

Figure 5 shows very little dust in general in ESO184-G82, and also only minor evidence for dust at the spaxel closest to the actual GRB/SN position ($E_{B-V} = 0.04 \pm 0.03\,\mathrm{mag}$, or $A_V = 0.13 \pm 0.09\,\mathrm{mag}$) and its immediate environment ($E_{B-V} = 0.03^{+0.05}_{-0.03}\,\mathrm{mag}$ in the 9 spaxels closest to the GRB/SN position). The only locations where we observe significant dust reddening are the centers of H ıı regions as exemplified by the WR region (Fig. 5). They show a centrally-symmetric substructure in dust extinction decreasing from the inside out and peaking at $E_{B-V} \sim 0.25\,\mathrm{mag}$ or $A_V = 0.8\,\mathrm{mag}$. A galaxy-integrated spectrum yields $E_{B-V} = 0.05 \pm 0.02\,\mathrm{mag}$, or $A_V = 0.15 \pm 0.06\,\mathrm{mag}$, which is in remarkable agreement with the average optical depth τ_V derived from modeling the UV-to-radio spectral energy distribution (Michałowski et al. 2014).
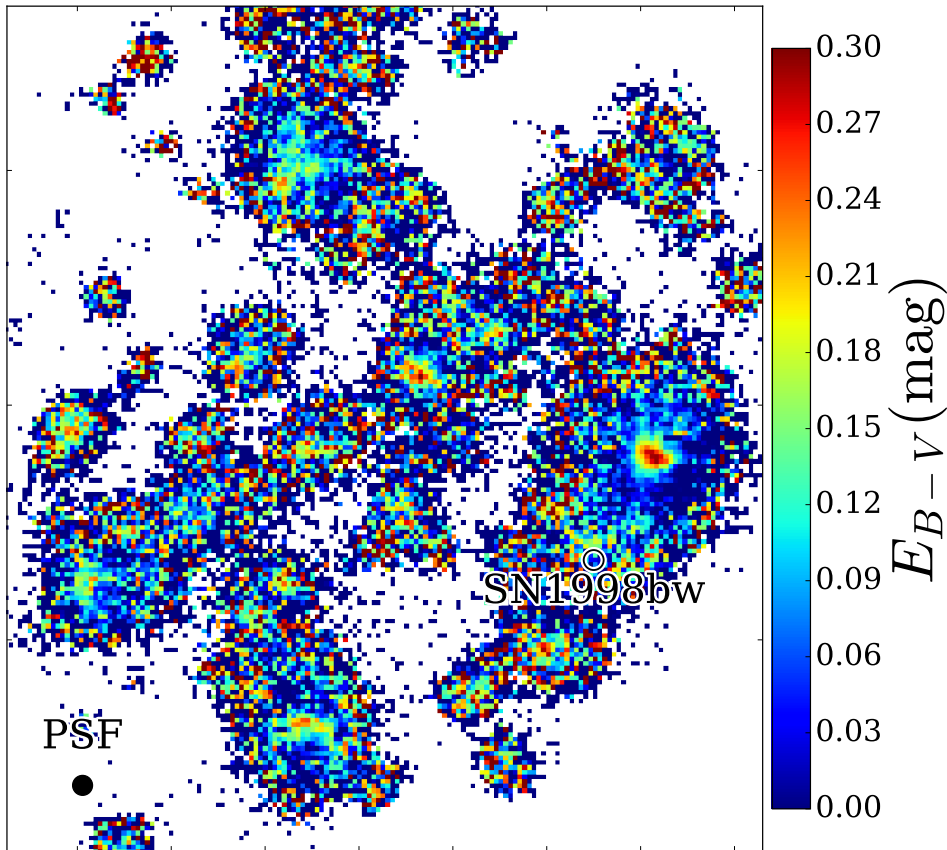
Fig. 5: Dust-reddening distribution in ESO184-G82 as measured through the Balmer decrement. We only show spaxels in which Hβ is detected with a significance of at least 3 σ. The shown image spans 34" by 38", or 6.1 by 6.8 kpc. The circle denoting the position of SN 1998bw has a **diameter** of 160 pc.

These low dust reddening values are somewhat in tension to results from optical spectroscopy in previous works (Hammer et al. 2006; Christensen et al. 2008). While we can reproduce our MUSE values with a re-reduction of the archival data used in Hammer et al. (2006) as shown in Appendix A, the origin of the mismatch to the spatially-resolved data of Christensen et al. (2008) remains unclear[4].

Due to the reliable spectra-photometric calibration of the MUSE data (Sect. 3), our accurate stellar continuum modeling (Sect. 4.1), and the consistency with the **spatially-resolved dust properties from long-wavelength data (Michałowski et al. 2014)**, we believe that our new data now resolve the apparent conflict between an unexpectedly large reddening at the SN position derived in previous **works** and the SN itself, which did not show strong evidence of dust obscuration (e.g. Iwamoto et al. 1998; Patat et al. 2001). They provide further confidence in using SN 1998bw as an only mildly reddened SN template for comparison to other GRB/SNe (e.g. Zeh et al. 2004; Schulze et al. 2014; Kann et al. 2016, and references therein).

---

[4]Potential reasons include uncertainties in the flux calibration (Hα and Hβ are located in two different grism setting for VIMOS) or the Balmer dust correction (the disagreement between our and their values is highest where the Hβ flux is lowest).

4.4. Metallicity Diagnostics

4.4.1. Initial Considerations

Metal abundances of H ɪɪ-regions are a central observable to study cosmo-chemical evolution, and a large set of literature is devoted to the various possibilities, their advantages, and perils to infer abundances from H ɪɪ-region spectra (e.g. Pagel et al. 1979; McGaugh 1991; Pilyugin & Thuan 2005; Kewley & Ellison 2008). Very briefly, the most common methods to deduce chemical abundances, and from those, the abundance of oxygen (traditionally expressed in $12 + \log(O/H)$) make use of either photo-ionization models (e.g. Evans & Dopita 1985; Dopita et al. 2000; Kewley & Dopita 2002) or empirical correlations between certain strong-line ratios and oxygen abundances derived through electron temperatures T_e from collisionally-excited lines (CELs, e.g. Pettini & Pagel 2004; Marino et al. 2013). Commonly-used ratios are for example [N ɪɪ]/[O ɪɪ], [O ɪɪɪ]/[N ɪɪ], [N ɪɪ]/Hα, or $R_{23} = ([O ɪɪ]+[O ɪɪɪ])/H\beta$, which have been (re)-calibrated numerous times against different samples of T_e or photo-ionization models, yielding a large set of different calibrators in the literature (e.g. Kewley & Dopita 2002; Kobulnicky & Kewley 2004; Pilyugin & Thuan 2005; Nagao et al. 2006; Maiolino et al. 2008).

The most fundamental problem in using and interpreting the oxygen abundances derived in this way is that different methods are only very rarely consistent (e.g. Kewley & Ellison 2008) giving rise to the abundance determination problem (Peimbert 1967). Methods based on temperature-sensitive CELs typically show abundances that are lower by 0.2-0.4 dex with respect to photoionization-based methods or abundances derived using temperatures from recombination lines (e.g. López-Sánchez et al. 2012, and references therein), in particular in the high-metallicity region. A possible solution to the abundance determination problem are small-scale temperature fluctuations (e.g. Peimbert 2003; Esteban et al. 2004) or an electron population distributed somewhat differently than in thermal Maxwell-Boltzmann equilibrium (Nicholls et al. 2012; López-Sánchez et al. 2012), but until these discrepancies are fully resolved, element abundances from emission lines remain the subject of large controversy.

A second, independent problem relates to the observational difficulties in robustly measuring emission line fluxes for lines in different wavelength ranges for faint, high-redshift galaxies. Due to various observational constraints, the available data is typically limited to a handful of strong lines. This is similarly true for our observations here, as the MUSE data do not cover the strong [O ɪɪ]($\lambda\lambda3726, 3729$) doublet nor [O ɪɪɪ]($\lambda4363$), one of the most commonly-used, temperature-sensitive CEL. A very popular emission-line diagnostic in the literature has thus been the logarithm of the ratio of [O ɪɪɪ]/Hβ to [N ɪɪ]/Hα or short O3N2 (e.g. Pettini & Pagel 2004; Marino et al. 2013), because of its independence on dust reddening and relative observational ease with which it can be measured even at $z \sim 2$.
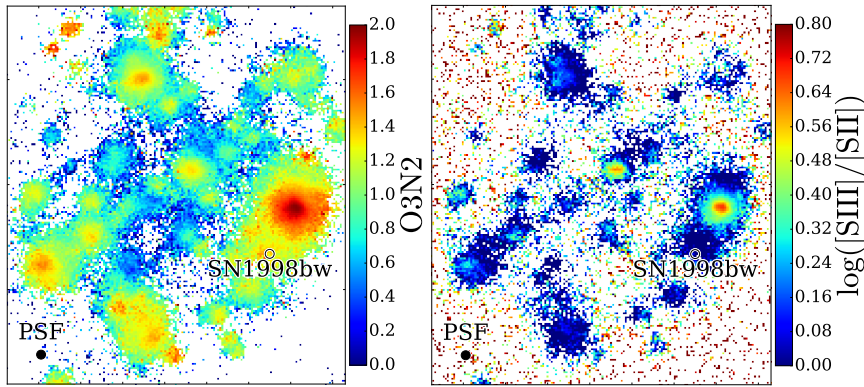
Fig. 6: Face-to-face comparison between the ESO184-G82 maps of O3N2, often used for abundance determinations and [S III]/[S II], a tracer of the ionization state of the hot gas. Only spaxels with **SNR > 3** are shown. Image dimensions are similar to Fig. 5.

4.4.2. Specific Problems of Empirical Metallicity Diagnostics

From the very different ionization potentials (IPs) of N and O^+ (14.5 eV versus 35.1 eV), it is **directly** clear that O3N2 should also carry a strong dependence on the ionization parameter in addition to its inverse proportionality to oxygen abundance (e.g. Alloin et al. 1979; Ho et al. 2015). In Fig. 6, we plot the O3N2 map of ESO184-G82, which immediately translates into a map of oxygen abundance ($12 + \log(O/H)$ would be lowest where O3N2 is highest) in common strong-line diagnostics (Pettini & Pagel 2004).

When inspecting the left part of Fig. 6, however, it becomes apparent that O3N2-based oxygen abundances (and similarly for those from N2) produce abundance maps that are hard to understand in a physical context: O3N2 varies significantly on $\lesssim$ kpc scales leading to an unexpected[5] chemically inhomogeneous structure within individual H II regions with their central abundances up to 0.3 dex lower than their outer edges. However, we believe that the significant gradients in O3N2/N2 observed in most of the H II regions are unlikely due to a genuine variation in oxygen abundance but are more likely the effect of a changing ionization parameter on O3N2/N2. We will explore this hypothesis further in the following sections.

4.4.3. Ionization Map

Our MUSE data is of sufficient depth and quality to test how strongly O3N2 is affected by ionization empirically through the ratio of [S III] (IP = 23.3 eV) to [S II] (IP = 10.3 eV), widely considered as one of the best tracers of the ionization parameter (Diaz et al. 1991) as it shows in contrast to [O III]/[O II] only very little dependence on abundance itself (Kewley & Dopita 2002; Dors et al. 2011). The resulting map[6] is shown in Fig. 6 and clearly highlights that the center of the H II regions have the largest values of [S III]/[S II], and thus ionization parameter.

---

[5]Despite the filamentary structure of nearby giant H II regions like 30 Doradus, they are usually adequately described with abundances that are homogeneous throughout the region (e.g. Pellegrini et al. 2011, and references therein).

[6]As MUSE does not cover the wavelength range of [S III]($\lambda 9532$), we use a theoretical value of [S III]($\lambda 9532$) = $2.44 \times$ [S III]($\lambda 9069$) (Mendoza & Zeippen 1982) here.
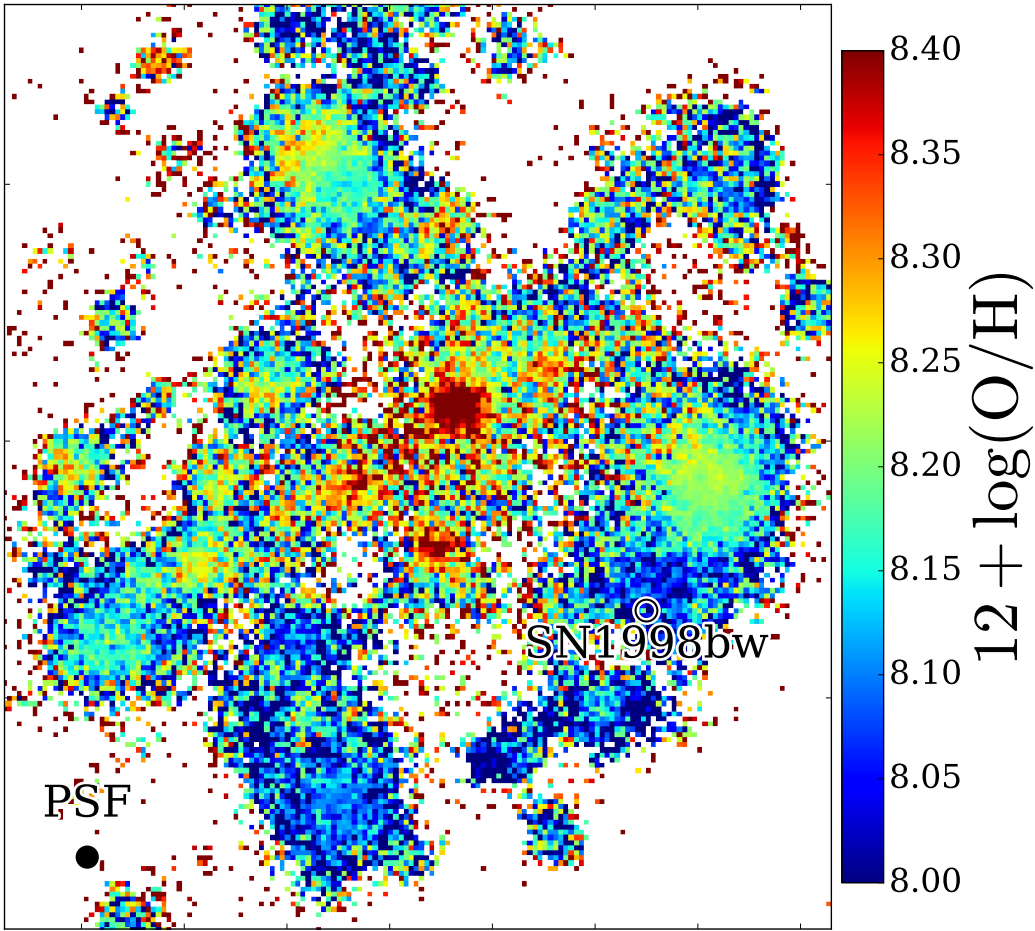
Fig. 7: Map of $12+\log(O/H)$ as obtained through the [S $\text{\textsc{ii}}$] and [N $\text{\textsc{ii}}$] based method of Dopita et al. (2016). Only spaxels with **SNR > 3** are shown. Image dimensions are 34" by 38", or 6.1 kpc by 6.8 kpc, similar to Fig. 5. The circle denoting the position of SN 1998bw has a diameter of 160 pc. Abundance determination methods via lines that are sensitive to electron temperature return values that are $0.1 - 0.2$ dex higher.

This adds further support to our initial conjecture, and ascertains that the radially symmetric structure of individual H $\text{\textsc{ii}}$-regions in the O3N2 map is due to an increase of the ionization parameter towards the center and not a decrease in chemical abundance. Simple O3N2 (or N2-based) diagnostic line ratios are thus inadequate to produce accurate maps of oxygen abundance at the level of detail of our MUSE data (see also Appendix B). Comparing the specific measurements of oxygen abundance in Table 1, it becomes clear that O3N2 systematically under/overestimates $12 + \log(O/H)$ in regions of higher (as in the WR region) or lower ionization parameter (as at the explosion site), respectively.

4.4.4. Metallicity Map

After rejecting common empirical methods using O3N2 or N2 as accurate metallicity tracer due to their ionization dependence, we turn to diagnostics based on photo-ionization models. Unfortunately, most of the previous strong-line methods rely in one way or another on the strong [O $\text{\textsc{ii}}$]$(\lambda\lambda3726,3729)$ doublet(Kewley & Dopita 2002), which is not directly available to us here.

Also [S III]/[S II] is a good ionization tracer, but [S III] is relatively faint and not detected in most of our spaxels (see Fig. 6).

A recently published method based on photo-ionization modeling (Dopita et al. 2016) seems to perfectly fit to our data: it relies solely on Hα, [N II], and [S II], which are all strong and well within the wavelength range of MUSE. The method, D16, is introduced as "effectively independent of both ionization parameter and ISM pressure" (Dopita et al. 2016), and Fig. 7 displays the respective map of 12 + log(O/H) in regions where all necessary lines are detected at a signal-to-noise ratio of at least 3.

Clearly, the strong abundance gradient over individual H II-regions as would have been deduced from O3N2, is not observed in this diagnostic. Instead, the oxygen abundance map displays a relatively smooth behavior with a decreasing overall metallicity from the center of the galaxy towards the outside (see also Sect. 4.5). The spaxel abundance at the SN position is 12 + log(O/H) = 8.00 or $0.20\,Z_\odot$. The immediate environment is consistent with this value and homogeneous: spaxels within a radius of 70 pc to the SN position yield 12 + log(O/H) = 8.04 ± 0.06. The WR region displays a somewhat higher oxygen abundance with $12 + \log(\text{O/H}) = 8.22 \pm 0.03$ or $0.34 \pm 0.03\,Z_\odot$ around the peak of the Hα emission.

It is of course reasonable to ask now whether the new Dopita et al. (2016) diagnostic provides more reliable constraints on oxygen abundance than previous methods given the significant differences that exists between all of them (Bian et al. 2017). In addition, for low-mass galaxies as is the case here, this diagnostic seems to return lower oxygen abundances than previous methods (Kashino et al. 2016). To elaborate further on the [S II]-based diagnostic, we reproduce the combined Eq. 1 and 2 from Dopita et al. (2016)

$$12 + \log(\text{O/H}) = 8.77 + \log([\text{N II}]/[\text{S II}]) + 0.264 \log([\text{N II}]/\text{H}\alpha) \tag{1}$$

with [N II] being the flux in the [N II]($\lambda6484$) line, and [S II] the flux in the [S II]($\lambda\lambda6717, 6731$) doublet. The primary observable is thus the nitrogen to sulfur ratio, which is a tracer of the nitrogen to oxygen ratio[7]. Because nitrogen is also produced in intermediate mass stars, N/O starts to depend on 12+log(O/H) above 12+log(O/H) ~ 7.8 (e.g. Izotov & Thuan 1999; Pérez-Montero et al. 2013, 2016), and as expected, a N/O map via Amorín et al. (2010) is very similar to the map of oxygen abundance in the respective strong line diagnostic.

The map of oxygen abundance then fundamentally relies on the N/O-to-O/H, calibration, and it is in principle not impossible that the applied calibration is slightly offset, in particular in the low-metallicity region. However, the calibration sample for N/O-to-O/H in the metallicity range of interest is based on low-metallicity blue compact dwarf galaxies (Izotov & Thuan 1999), not dissimilar in physical properties to our **galaxy**. In addition, there could also be internal variations

---

[7]Sulfur and oxygen are both α-process elements produced in massive stars, and observed to track each other well in different environments (see e.g. Fig. 6 in Izotov et al. 2006).
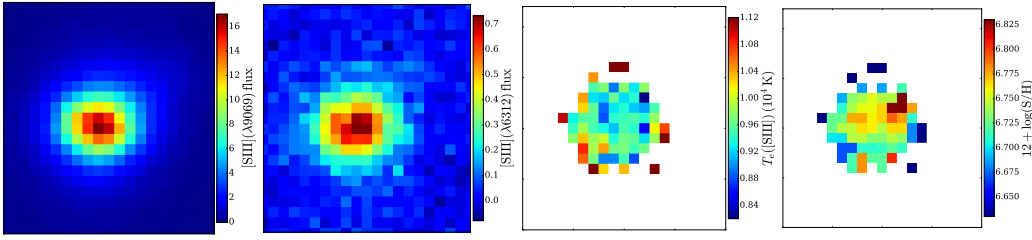
Fig. 8: Estimation of electron temperature $T(e)$ through [S III] and sulfur abundance in the WR region. top-left: nebular [S III]($\lambda9069$), top-right: auroral [S III]($\lambda6312$), bottom-left: [S III] electron temperatures, bottom-right: $12 + \log(S/H)$ as derived from the electron temperature. The solar abundance [O/S] is 1.57 (Asplund et al. 2009), so the $12 + \log(S/H)$ scale corresponds to $12 + \log(O/H) = 8.2$ to 8.4. All panels are approximately 6" × 6", or 1 kpc × 1 kpc in size. One MUSE spaxel corresponds to 35 pc.

in N/O at a given $12 + \log(O/H)$, or differences between the host of SN 1998bw to the calibration sample. For example, infall of primordial gas (e.g., Michałowski et al. 2015) would decrease $12 + \log(O/H)$, but leave N/O unaffected (Kashino et al. 2016). Another point of concern would be an anomalously high N/O ratio for the SN region as claimed by Hammer et al. (2006). Both of these effects would lead us to over-predict the actual oxygen abundance in the SN region via the Dopita et al. (2016) diagnostic. **However, the oxygen abundances derived via Eq. 1 are already lower than the values from temperature-sensitive collisionally-excited lines (Sect. 4.4.5), which are sensitive to the actual oxygen abundance. We hence find no evidence for a systematic overestimation of the metallicity in the D16 scale at either the explosion site or the WR region.**

4.4.5. Metallicities Based on Electron Temperatures

Given the strong constraints that these measurements of oxygen abundance could imply for the SN 1998bw progenitor metallicity, we further seek to corroborate our earlier abundances through those from temperature-sensitive lines. Unfortunately, the brightest and most-commonly used auroral line [O III]($\lambda4363$) is not covered by the MUSE wavelength response, and the other temperature-sensitive lines are too faint to be detected in most of the individual spaxels. However, we clearly detect [S III]($\lambda6312$) both in the WR region (Fig. 8), and in integrated spectra around the SN position.

Following Nicholls et al. (2013), we derive an electron temperature T_e using [S III] in the central part of the WR region of around $T_e([S III]) = (0.94 \pm 0.02) \cdot 10^4$ K. Figure 8 contains maps of the crucial emission lines (nebular [S III]($\lambda9069$), and auroral [S III]($\lambda6312$)), the resulting temperatures as well as sulfur abundances. These values correspond to somewhat larger temperatures of [O III] of around $T_e([O III]) \sim 1.07 \cdot 10^4$ K (Izotov et al. 2006; Binette et al. 2012). The flux in the doublets of [O II]($\lambda\lambda7320,7330$), [O III]($\lambda\lambda4959,5007$) and Hβ then yields central abundances of the WR region around $12 + \log(O/H) \sim 8.3$.

Similar values are obtained when using solar abundances to convert the sulfur to an oxygen abundance. These are slightly ($0.1 - 0.2$ dex) higher than those implied by the strong line diagnostic from Sect. 4.4.4, but critically depend on the sulfur-to-oxygen temperature conversion or assumed

abundance. They are thus subject to some systematic uncertainties. However, it is clear that the strong structure in O3N2 or N2 over the H ɪɪ-region are not observed in electron temperatures.

Emission-lines at the explosion site are substantially fainter, and [S ɪɪɪ](λ6312) is only detected in a stacked spectrum extracted from 3×3 spaxels around the SN position which yields T_e([S ɪɪɪ]) = $(1.24 \pm 0.18) \cdot 10^4$ K. This is slightly higher than in the WR region, but with large uncertainties. The corresponding oxygen abundance derived in a similar manner as above is $12 + \log(O/H) = 7.92 \pm 0.27$.

We also reduce public archival VLT/FORS2 long-slit spectroscopy (Appendix A) as it covers both WR region and SN position and extends below 4000 Å. Using the well-detected [O ɪɪɪ](λ4363) line, we measure temperatures of T_e([O ɪɪɪ]) = $(1.05 \pm 0.05) \cdot 10^4$ K and T_e([O ɪɪɪ]) = $(1.29 \pm 0.18) \cdot 10^4$ K for the WR and SN region, broadly consistent with the estimates from MUSE through [S ɪɪɪ](λ6312). They imply oxygen abundances of $12 + \log(O/H) = 8.36 \pm 0.07$ and 8.09 ± 0.15 for WR and SN region, respectively.

Our relatively low oxygen abundances at the location of explosion site, WR region, as well as the galaxy integrated value ($12 + \log(O/H) \sim 8.3$, Sect. 4.6) correspond to 0.2 to 0.5 times the solar value, and thus explain many of the long-wavelength properties of ESO184-G82 as typical for metal-poor dwarf galaxies without invoking a deficiency in molecular gas (Michałowski et al. 2016).

4.5. Metallicity Gradient

The metallicity of galaxies is often observed to decrease with the distance from their centers (e.g. Zaritsky et al. 1994; Sánchez et al. 2014), also seen in the hosts of SNe (Galbany et al. 2016b) or here (Fig. 7). These gradients are important to understand for spatially-unresolved studies at high redshift, where positional offsets can be measured, but abundances are only derived in a galaxy integrated manner.

Using a linear regression on the data of Fig. 9, the metallicity gradient is best fit with a slope of -0.25 ± 0.02 dex/R_{25} in relative, or -0.06 dex kpc^{-1} in physical scales, well in the range that was previously reported for galaxies of comparable stellar mass (Ho et al. 2015). Here, R_{25} is the radius at the $B = 25$ mag arcsec^2 isophote. O3N2-based diagnostics return slightly steeper, but within errors generally compatible values. The linear fit to the oxygen abundance data is a reasonable description of the data, except for the very center (deprojected distance < 1 kpc), where the metallicity is seen to decrease more steeply. Limiting the fit range to this region, the slope in the central kpc is -0.18 dex kpc^{-1} (see dashed line in Fig. 9), but depends strongly on the metallicity diagnostic[8].

---

[8]A O3N2-based method returns a decreasing abundance towards the center, similar to what is seen also in a third of SN hosts in this diagnostic (Galbany et al. 2016b).
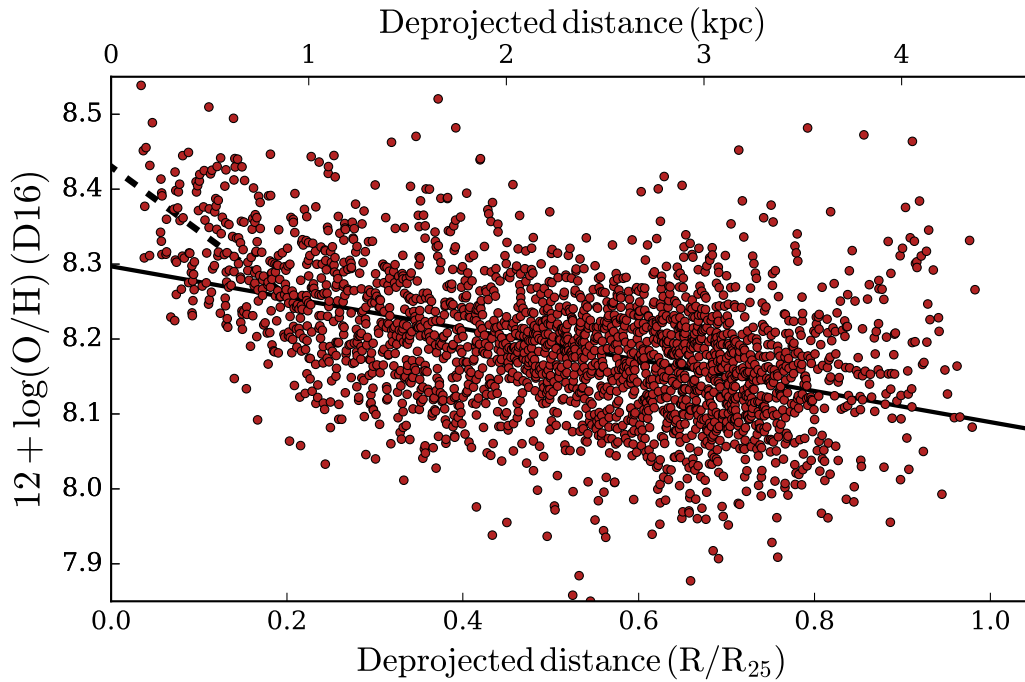
Fig. 9: Metallicity gradient for ESO184-G82 in the Dopita et al. (2016) scale. Each data point is a spaxel-based measurement of oxygen-abundance, where individual spaxels have been binned with their direct neighbors to enhance the signal-to-noise ratio if necessary.

A comparison between this metallicity gradient to the typical values of (projected) GRB distances from the galaxy centers[9] of 1.3 kpc (Blanchard et al. 2016) does not provide strong reason to suggest that the average measurement of GRB host metallicities from spatially-unresolved data is significantly skewed when compared to the GRB site metallicity. There is, however, a non-negligible fraction of GRBs at substantial distances to their hosts (10% at > 3 kpc) where metallicity gradients might lead to overestimates of the GRB site abundance from unresolved spectra for single objects.

4.6. ESO184-G82 if Seen at High Redshift

GRB 980425 is the closest GRB since the discovery of GRB afterglows, and an exceptional opportunity to measure the physical parameters of its host with high precision and high spatial resolution. Typically, information on the environments of GRBs or similar kind of transients at higher redshift is obtained only through galaxy-integrated measurements (Krühler et al. 2015; Japelj et al. 2016; Vergani et al. 2017), where it is not necessarily obvious whether the measured parameters actually correspond to GRB/SN location properties. **We thus compare the physical parameters derived from the explosion site spectrum, the WR region (both extracted from the 9 closest spaxels to the SN position and WR region center) to those obtained from a galaxy-integrated spectrum of ESO184-G82. The latter is a simple sum of all spaxels within a radius of 25″**

---

[9]**GRBs are commonly found in dwarf galaxies with an irregular morphology (e.g., Fruchter et al. 2006; Lyman et al. 2017). Galaxy centers and thus positional offsets are hence sometimes difficult to determine robustly.**

around the galaxy's center, which should mimic how the galaxy would appear if it were unresolved and at high redshift.

First, we measure the total star-formation rate of ESO184-G82 by adding up the Hα flux of all individual spaxels after the respective spaxel-based reddening correction, which yields $SFR = 0.22 \pm 0.02 \, \mathrm{M_\odot \, yr^{-1}}$. If we instead use the Hα flux from the galaxy-integrated spectrum and then apply a single reddening correction, we derive $SFR = 0.17 \pm 0.02 \, \mathrm{M_\odot \, yr^{-1}}$. Both values agree with far-infrared, [O I], and [C II] -based SFRs (Michałowski et al. 2014, 2016), and the narrow-band Hα image from Sollerman et al. (2005) once their Salpeter IMF is taken into account (see also Savaglio et al. 2009). The difference to other Hα -based SFR measurements (Hammer et al. 2006; Christensen et al. 2008) is entirely due to either an overestimated dust correction or a different IMF.

We then obtain further physical parameters from the extracted spectra of the explosion site, the central part of the Wolf-Rayet region, and the integrated galaxy spectrum as summarized in Table 1. Generally, there is decent agreement between many of the physical properties of the galaxy and the SN site spectrum. Not unexpectedly, resolved measurement of EWs are significantly higher, whereas both dust reddening (by 0.03 mag) and oxygen abundance (by $0.1 - 0.2$ dex) are marginally lower at the explosion site than for a galaxy integrated spectrum. However, ESO184-G82 does not provide strong evidence that GRB position spectra are markedly different from galaxy-integrated values except for the obvious mismatch in equivalent width measurements. Whether this observation remains valid for a larger sample of GRB hosts remains to be seen, of course.

Comparing Table 1 with Fig. 7 and Fig. 9 also illustrates that the oxygen abundance derived from a galaxy-integrated spectrum is not the central abundance of the galaxy (see also e.g., Galbany et al. 2016b). As the metallicity determination in an unresolved case is a SFR-weighted measurement, it is dominated by H II-regions that are primarily located somewhat offset from the center as illustrated in Fig. 4 in this case and corresponds to a measurement at a distance of around 2 kpc to 3 kpc from the center of ESO184-G82.

GRB positions in general tend to be highly concentrated on the UV-brightest regions of their hosts (e.g., Svensson et al. 2010; Blanchard et al. 2016; Lyman et al. 2017). These are the same regions that will dominate the nebular-line emission in an unresolved, SFR-weighted spectrum from which physical parameters such as metallicity are typically inferred at higher redshift.

5. Conclusions and Summary

SN 1998bw represented the first solid observational evidence that linked GRBs with core-collapse supernovae, and since then has become the prototypical GRB/SN in terms of luminosity as well as spectral and temporal evolution. This very first GRB/SN has already demonstrated the absence of hydrogen and helium as well as the presence of broad absorption lines characteristic of a photosphere expanding at high velocities that should become typical of SNe following long GRBs in the later years.

Table 1: Physical properties inferred from MUSE/VLT IFU spectroscopy for the GRB 980425/SN 1998bw host galaxy ESO184-G82

	ESO184-G82	SN region	WR region
EW(Hα) (Å)	56.0 ± 1.4	92 ± 15	> 900
EW([O III]) (Å)	34.5 ± 0.9	54 ± 5	> 850
E_{B-V} (mag)	0.06 ± 0.02	$0.03^{+0.05}_{-0.03}$	0.22 ± 0.02
n_e (cm^{-3})[a]	80 ± 10	90 ± 10	150 ± 10
T_e([S III]) (10^4 K)[b]	⋯	1.24 ± 0.18	0.94 ± 0.02
T_e([O III]) (10^4 K)[b,c]	⋯	1.29 ± 0.18	1.05 ± 0.02
12 + log(O/H) (D16)[b]	8.13 ± 0.01	8.04 ± 0.06	8.22 ± 0.03
12 + log(O/H) (PP04, O3N2)[b]	8.31 ± 0.01	8.31 ± 0.01	8.11 ± 0.01
12 + log(O/H) (PP04, N2)[b]	8.33 ± 0.01	8.32 ± 0.01	8.18 ± 0.01
12 + log(O/H) (T_e)[c]	⋯	8.09 ± 0.15	8.36 ± 0.07
SFR (M$_\odot$ yr^{-1})	0.22 ± 0.02	⋯	⋯

Notes. [a] Derived from the [S II]($\lambda\lambda6716, 6731$) doublet ratio. [b] The quoted error is statistical only. There is an additional systematic error in each of these measurements due to various reasons. For the respective parameters, it is approximately $T_e = 0.1 \cdot 10^4$ K, 12 + log(O/H) (PP04, O3N2)=0.14 dex, 12 + log(O/H) (PP04, N2)=0.18 dex. The systematic error on 12 + log(O/H) (D16) is presently not well quantified, but we expect it in the range of ~0.1 dex. [c] Partially derived from the VLT/FORS2 spectra (Appendix A).

In this article, we use spatially-resolved spectroscopy obtained with the novel integral-field spectrograph MUSE at the VLT to study the properties of the hot gas phase and the stellar population in the SN 1998bw host galaxy with a particular **emphasis** on the SN position. Our data cover the largest fraction of the host galaxy with individual spaxels of 35×35 pc. The effective size of a spatial resolution element is limited by the atmospheric conditions and has a full-width half-maximum of 160 **pc**. The main results derived from this analysis can be summarized as follows:

(i) GRB 980425/SN 1998bw exploded in a young $(5 - 8$ Myr) and dust-poor $(E_{B-V} = 0.03^{+0.05}_{-0.03}$ mag) environment. The age of the stellar population corresponds to life times of stars with M_{ZAMS} between approximately 25 M$_\odot$ and 40 M$_\odot$. Our measurement of dust reddening for the explosion site is significantly lower than previous estimates and resolves the mismatch between an apparently dust-rich environment and a non-extinguished SN light curve.

(ii) The Wolf-Rayet region at a projected distance of 860 pc to the GRB explosion site is extremely young $(< 3$ Myr). This young age would imply implausibly high peculiar velocities for runaway stars and makes scenarios where the GRB progenitor is ejected from the WR region quite contrived. The progenitor mass obtained from modeling the SN 1998bw's nebular spectra (Maeda et al. 2006) is consistent with the one derived from the explosion environment and inconsistent with an origin in the WR region. This strongly suggests that the GRB formed in situ.

(iii) The total, dust-corrected SFR of ESO184-G82 is $SFR = 0.22 \pm 0.02$ M$_\odot$ yr^{-1} inferred from integrating the dust-corrected Hα flux in the respective spaxels. The galaxy has a metallicity gradient of -0.06 dex kpc^{-1}, suggesting that the typical offsets of at most few kpc for higher-redshift GRBs have a relatively small impact on the abundance determination for high-redshift GRB hosts on average.

(iv) Emission-line-based parameters, except equivalent widths, that are inferred from an integrated spectrum of the complete galaxy are dominated by the most star-forming regions and can thus lead to an adequate representation of the actual GRB explosion site properties.

Despite a considerable systematic uncertainty stemming from the validity and accuracy of specific strong-line metallicity diagnostics, we reach here the following robust conclusions with respect to abundances:

(v) Empirical strong-line methods using [O III]/Hβ and/or [N II]/Hα fail to produce accurate maps of metallicity at the level of detail probed by our MUSE observation. They significantly under/overestimate $12 + \log(\mathrm{O/H})$ in regions of high/low ionization parameter, respectively, and therefore return an unphysical radial gradient in individual H II-regions with their centers appearing artificially deprived in metals.

(vi) A recent method based on photoionization models and [S II] from Dopita et al. (2016) does not show an obvious dependence of inferred abundance on ionization and returns values that are broadly similar, but somewhat lower (by 0.1 dex to 0.2 dex) than those from electron temperatures via the observed ratios of auroral-to-nebular [S III] or [O III].

(vii) Taking the **above** considerations into account, we consider $12 + \log(\mathrm{O/H}) \sim 8.2$ at the SN position, $12 + \log(\mathrm{O/H}) \sim 8.3$ for a galaxy integrated spectrum and $12 + \log(\mathrm{O/H}) \sim 8.4$ for the nearby WR region as our best estimates of the respective oxygen abundances[10].

The immediate environment of GRB 980425 thus indicates a progenitor with $Z \sim 0.3\,Z_\odot$ and M_{ZAMS} between $\sim 25\,\mathrm{M}_\odot$ and $\sim 40\,\mathrm{M}_\odot$. Despite the preeminent efficiency, sensitivity and optical quality of MUSE, similar studies for a larger sample of GRB hosts remain observationally challenging due to the limitations in image quality implied by atmospheric turbulence. However, MUSE will soon be equipped with an adaptive optics module, with which the achievable spatial resolution could decrease to $0\rlap{.}''3$ over the $1' \times 1'$ field of view. This brings similar studies **(e.g., Izzo et al., in preparation)** into the realm of possibility for at least a handful of close GRBs and will allow us to reassess our constraints on GRB progenitors on a statistically more significant sample.

References

Alloin, D., Collin-Souffrin, S., Joly, M., & Vigroux, L. 1979, A&A, 78, 200

Amorín, R. O., Pérez-Montero, E., & Vílchez, J. M. 2010, ApJ, 715, L128

Anderson, J. P., Covarrubias, R. A., James, P. A., Hamuy, M., & Habergham, S. M. 2010, MNRAS, 407, 2660

Appenzeller, I., Fricke, K., Fürtig, W., et al. 1998, The Messenger, 94, 1

Arabsalmani, M., Roychowdhury, S., Zwaan, M. A., Kanekar, N., & Michałowski, M. J. 2015, MNRAS, 454, L51

Asplund, M., Grevesse, N., Sauval, A. J., & Scott, P. 2009, ARA&A, 47, 481

---

[10]**These values are based on the Dopita et al. (2016) diagnostic, but scaled upwards by 0.15 dex as indicated by the corresponding T_e abundances.**

Bacon, R., Accardo, M., Adjali, L., et al. 2010, in Proc. SPIE, Vol. 7735, Ground-based and Airborne Instrumentation for Astronomy III, 773508

Baldwin, J. A., Phillips, M. M., & Terlevich, R. 1981, PASP, 93, 5

Banerjee, S., Kroupa, P., & Oh, S. 2012, ApJ, 746, 15

Bian, F., Kewley, L. J., Dopita, M. A., & Blanc, G. A. 2017, ApJ, 834, 51

Binette, L., Matadamas, R., Hägele, G. F., et al. 2012, A&A, 547, A29

Blanchard, P. K., Berger, E., & Fong, W.-f. 2016, ApJ, 817, 144

Brinchmann, J., Pettini, M., & Charlot, S. 2008, MNRAS, 385, 769

Bruzual, G. & Charlot, S. 2003, MNRAS, 344, 1000

Chabrier, G. 2003, PASP, 115, 763

Chen, T.-W., Smartt, S. J., Bresolin, F., et al. 2013, ApJ, 763, L28

Christensen, L., Vreeswijk, P. M., Sollerman, J., et al. 2008, A&A, 490, 45

Cid Fernandes, R., Mateus, A., Sodré, L., Stasińska, G., & Gomes, J. M. 2005, MNRAS, 358, 363

Cid Fernandes, R., Schoenell, W., Gomes, J. M., et al. 2009, in Rev. Mex. Astron. Astrofis. Conf. Ser., Vol. 35, 127–132

Clocchiatti, A., Suntzeff, N. B., Covarrubias, R., & Candia, P. 2011, AJ, 141, 163

Diaz, A. I., Terlevich, E., Vilchez, J. M., Pagel, B. E. J., & Edmunds, M. G. 1991, MNRAS, 253, 245

Dopita, M. A., Kewley, L. J., Heisler, C. A., & Sutherland, R. S. 2000, ApJ, 542, 224

Dopita, M. A., Kewley, L. J., Sutherland, R. S., & Nicholls, D. C. 2016, Ap&SS, 361, 61

Dors, Jr., O. L., Krabbe, A., Hägele, G. F., & Pérez-Montero, E. 2011, MNRAS, 415, 3616

Eldridge, J. J., Langer, N., & Tout, C. A. 2011, MNRAS, 414, 3501

Erb, D. K., Shapley, A. E., Pettini, M., et al. 2006, ApJ, 644, 813

Esteban, C., Peimbert, M., García-Rojas, J., et al. 2004, MNRAS, 355, 229

Evans, I. N. & Dopita, M. A. 1985, ApJS, 58, 125

Fagotto, F., Bressan, A., Bertelli, G., & Chiosi, C. 1994, A&AS, 105

Förster Schreiber, N. M., Genzel, R., Bouché, N., et al. 2009, ApJ, 706, 1364

Fruchter, A. S., Levan, A. J., Strolger, L., et al. 2006, Nature, 441, 463

Fynbo, J. P. U., Jakobsson, P., Prochaska, J. X., et al. 2009, ApJS, 185, 526

Fynbo, J. U., Holland, S., Andersen, M. I., et al. 2000, ApJ, 542, L89

Galama, T. J., Vreeswijk, P. M., van Paradijs, J., et al. 1998, Nature, 395, 670

Galbany, L., Anderson, J. P., Rosales-Ortega, F. F., et al. 2016a, MNRAS, 455, 4087

Galbany, L., Stanishev, V., Mourão, A. M., et al. 2014, A&A, 572, A38

Galbany, L., Stanishev, V., Mourão, A. M., et al. 2016b, A&A, 591, A48

González Delgado, R. M., Leitherer, C., & Heckman, T. M. 1999, ApJS, 125, 489

Graham, J. F. & Fruchter, A. S. 2013, ApJ, 774, 119

Hammer, F., Flores, H., Schaerer, D., et al. 2006, A&A, 454, 103

Hjorth, J. & Bloom, J. S. 2012, The Gamma-Ray Burst - Supernova Connection, 169–190

Ho, I.-T., Kudritzki, R.-P., Kewley, L. J., et al. 2015, MNRAS, 448, 2030

Hoogerwerf, R., de Bruijne, J. H. J., & de Zeeuw, P. T. 2001, A&A, 365, 49

Hunter, J. D. 2007, Computing In Science & Engineering, 9, 90

Iwamoto, K., Mazzali, P. A., Nomoto, K., et al. 1998, Nature, 395, 672

Izotov, Y. I., Stasińska, G., Meynet, G., Guseva, N. G., & Thuan, T. X. 2006, A&A, 448, 955

Izotov, Y. I. & Thuan, T. X. 1999, ApJ, 511, 639

Japelj, J., Vergani, S. D., Salvaterra, R., et al. 2016, A&A, 590, A129

Kann, D. A., Schady, P., Olivares E., F., et al. 2016, A&A, submitted [arXiv:1606.06791]

Kashino, D., Renzini, A., Silverman, J. D., & Daddi, E. 2016, ApJ, 823, L24

Kennicutt, Jr., R. C. 1998, ARA&A, 36, 189

Kewley, L. J. & Dopita, M. A. 2002, ApJS, 142, 35

Kewley, L. J., Dopita, M. A., Leitherer, C., et al. 2013, ApJ, 774, 100

Kewley, L. J. & Ellison, S. L. 2008, ApJ, 681, 1183

Kobulnicky, H. A. & Kewley, L. J. 2004, ApJ, 617, 240

Krühler, T., Fynbo, J. P. U., Geier, S., et al. 2012a, A&A, 546, A8

Krühler, T., Malesani, D., Fynbo, J. P. U., et al. 2015, A&A, 581, A125

Krühler, T., Malesani, D., Milvang-Jensen, B., et al. 2012b, ApJ, 758, 46

Kulkarni, S. R., Frail, D. A., Wieringa, M. H., et al. 1998, Nature, 395, 663

Kuncarayakti, H., Doi, M., Aldering, G., et al. 2013a, AJ, 146, 30

Kuncarayakti, H., Doi, M., Aldering, G., et al. 2013b, AJ, 146, 31

Kuncarayakti, H., Galbany, L., Anderson, J. P., Krühler, T., & Hamuy, M. 2016, A&A, 593, A78

Lauberts, A. & Valentijn, E. A. 1989, The surface photometry catalogue of the ESO-Uppsala galaxies

Le Floc'h, E., Charmandaris, V., Gordon, K., et al. 2012, ApJ, 746, 7

Leloudas, G., Gallazzi, A., Sollerman, J., et al. 2011, A&A, 530, A95

Leloudas, G., Schulze, S., Krühler, T., et al. 2015, MNRAS, 449, 917

Levesque, E. M., Berger, E., Soderberg, A. M., & Chornock, R. 2011, ApJ, 739, 23

Levesque, E. M. & Leitherer, C. 2013, ApJ, 779, 170

Li, W., Leaman, J., Chornock, R., et al. 2011, MNRAS, 412, 1441

López-Sánchez, Á. R., Dopita, M. A., Kewley, L. J., et al. 2012, MNRAS, 426, 2630

Lunnan, R., Chornock, R., Berger, E., et al. 2014, ApJ, 787, 138

Lyman, J. D., Levan, A. J., Tanvir, N. R., et al. 2017, MNRAS[arXiv:1701.05925]

Maeda, K., Nomoto, K., Mazzali, P. A., & Deng, J. 2006, ApJ, 640, 854

Maiolino, R., Nagao, T., Grazian, A., et al. 2008, A&A, 488, 463

Marino, R. A., Rosales-Ortega, F. F., Sánchez, S. F., et al. 2013, A&A, 559, A114

Mazzali, P. A., Nomoto, K., Patat, F., & Maeda, K. 2001, ApJ, 559, 1047

McGaugh, S. S. 1991, ApJ, 380, 140

Mendoza, C. & Zeippen, C. J. 1982, MNRAS, 199, 1025

Meynet, G. & Maeder, A. 2005, A&A, 429, 581

Michałowski, M. J., Castro Cerón, J. M., Wardlow, J. L., et al. 2016, A&A, 595, A72

Michałowski, M. J., Gentile, G., Hjorth, J., et al. 2015, A&A, 582, A78

Michałowski, M. J., Hjorth, J., Malesani, D., et al. 2009, ApJ, 693, 347

Michałowski, M. J., Hunt, L. K., Palazzi, E., et al. 2014, A&A, 562, A70

Modjaz, M., Kewley, L., Bloom, J. S., et al. 2011, ApJ, 731, L4

Morisset, C., Delgado-Inglada, G., Sánchez, S. F., et al. 2016, A&A, 594, A37

Nagao, T., Maiolino, R., & Marconi, A. 2006, A&A, 459, 85

Nicholls, D. C., Dopita, M. A., & Sutherland, R. S. 2012, ApJ, 752, 148

Nicholls, D. C., Dopita, M. A., Sutherland, R. S., Kewley, L. J., & Palay, E. 2013, ApJS, 207, 21

Osterbrock, D. E. 1989, Astrophysics of gaseous nebulae and active galactic nuclei

Osterbrock, D. E. & Ferland, G. J. 2006, Astrophysics of gaseous nebulae and active galactic nuclei

Pagel, B. E. J., Edmunds, M. G., Blackwell, D. E., Chun, M. S., & Smith, G. 1979, MNRAS, 189, 95

Patat, F., Cappellaro, E., Danziger, J., et al. 2001, ApJ, 555, 900

Pei, Y. C. 1992, ApJ, 395, 130

Peimbert, A. 2003, ApJ, 584, 735

Peimbert, M. 1967, ApJ, 150, 825

Pellegrini, E. W., Baldwin, J. A., & Ferland, G. J. 2011, ApJ, 738, 34

Perets, H. B. & Šubr, L. 2012, ApJ, 751, 133

Pérez-Montero, E., Contini, T., Lamareille, F., et al. 2013, A&A, 549, A25

Pérez-Montero, E., García-Benito, R., Vílchez, J. M., et al. 2016, A&A, 595, A62

Perley, D. A., Quimby, R. M., Yan, L., et al. 2016, ApJ, 830, 13

Pettini, M. & Pagel, B. E. J. 2004, MNRAS, 348, L59

Pilyugin, L. S. & Thuan, T. X. 2005, ApJ, 631, 231

Planck Collaboration. 2014, A&A, 571, A16

Prieto, J. L., Krühler, T., Anderson, J. P., et al. 2016, ApJ, 830, L32

Prieto, J. L., Stanek, K. Z., & Beacom, J. F. 2008, ApJ, 673, 999

Sánchez, S. F., Rosales-Ortega, F. F., Iglesias-Páramo, J., et al. 2014, A&A, 563, A49

Savaglio, S., Glazebrook, K., & Le Borgne, D. 2009, ApJ, 691, 182

Schady, P., Krühler, T., Greiner, J., et al. 2015, A&A, 579, A126

Schlafly, E. F. & Finkbeiner, D. P. 2011, ApJ, 737, 103

Schulze, S., Malesani, D., Cucchiara, A., et al. 2014, A&A, 566, A102

Smette, A., Sana, H., Noll, S., et al. 2015, A&A, 576, A77

Sollerman, J., Östlin, G., Fynbo, J. P. U., et al. 2005, New A, 11, 103

Soto, K. T., Lilly, S. J., Bacon, R., Richard, J., & Conseil, S. 2016, MNRAS, 458, 3210

Stasińska, G. 2006, A&A, 454, L127

Storey, P. J. & Zeippen, C. J. 2000, MNRAS, 312, 813

Svensson, K. M., Levan, A. J., Tanvir, N. R., Fruchter, A. S., & Strolger, L.-G. 2010, MNRAS, 405, 57

Tanvir, N. R., Fox, D. B., Levan, A. J., et al. 2009, Nature, 461, 1254

Thöne, C. C., Christensen, L., Prochaska, J. X., et al. 2014, MNRAS, 441, 2034

Thöne, C. C., de Ugarte Postigo, A., García-Benito, R., et al. 2015, MNRAS, 451, L65

Thöne, C. C., Fynbo, J. P. U., Östlin, G., et al. 2008, ApJ, 676, 1151

Tremonti, C. A., Heckman, T. M., Kauffmann, G., et al. 2004, ApJ, 613, 898

Vergani, S. D., Palmerio, J., Salvaterra, R., et al. 2017, A&A, 599, A120

Walt, S. v. d., Colbert, S. C., & Varoquaux, G. 2011, Computing in Science and Engg., 13, 22

Weilbacher, P. M., Streicher, O., Urrutia, T., et al. 2014, in ASP Conf. Ser., Vol. 485, Astronomical Data Analysis Software
    and Systems XXIII, ed. N. Manset & P. Forshay, 451

Wesson, R., Stock, D. J., & Scicluna, P. 2016, MNRAS, 459, 3475

Wiersema, K., Savaglio, S., Vreeswijk, P. M., et al. 2007, A&A, 464, 529

Xu, D., de Ugarte Postigo, A., Leloudas, G., et al. 2013, ApJ, 776, 98

Zaritsky, D., Kennicutt, Jr., R. C., & Huchra, J. P. 1994, ApJ, 420, 87

Zeh, A., Klose, S., & Hartmann, D. H. 2004, ApJ, 609, 952

List of Objects

Appendix A: Re-analysis of Archival Long-slit Spectra

The ESO archive contains a number of public, high signal-to-noise, but low-resolution spectra obtained with the FOcal Reducer/low dispersion Spectrograph 2 (FORS2, Appenzeller et al. 1998) that are particularly interesting in the context of this work. These are the same spectra used by Hammer et al. (2006), and were taken with a $1''\!.0$ slit on 2004-07-15 with the grism 600B (3450 Å to 6050 Å at a resolving power R of $R \sim 850$) and on 2004-07-16 with grism 600RI (5300 Å to 8450 Å and $R \sim 1050$). The position angle during both observations was 28° from East such that both the SN and WR region are covered by the slit (Fig. 1). The total exposure time was 1350 s (each three individual frames with 300 s and 150 s) in the 600B setup and 2250 s in the 600RI (each five single frames with 300 s and 150 s) setup. We reduce and analyze the archival FORS2 data using standard procedures, specifically the ESO FORS2 pipeline in its version `5.3.8` and self-written methods and algorithms in `python` (Krühler et al. 2015).
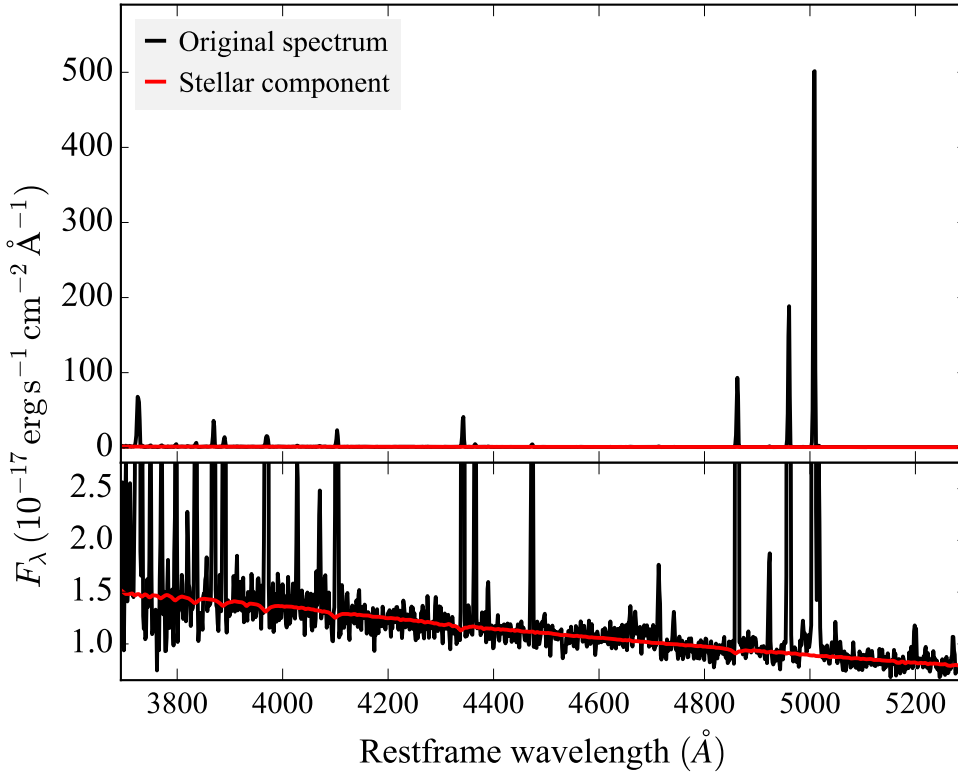
Fig. A.1: FORS2 600*B* spectrum of the brightest pixel of the WR region. **Black is the original spectrum and red represents the fitted stellar component. The *upper panel* shows the full flux range, while the *lower panel* is a zoom in to the stellar continuum.**
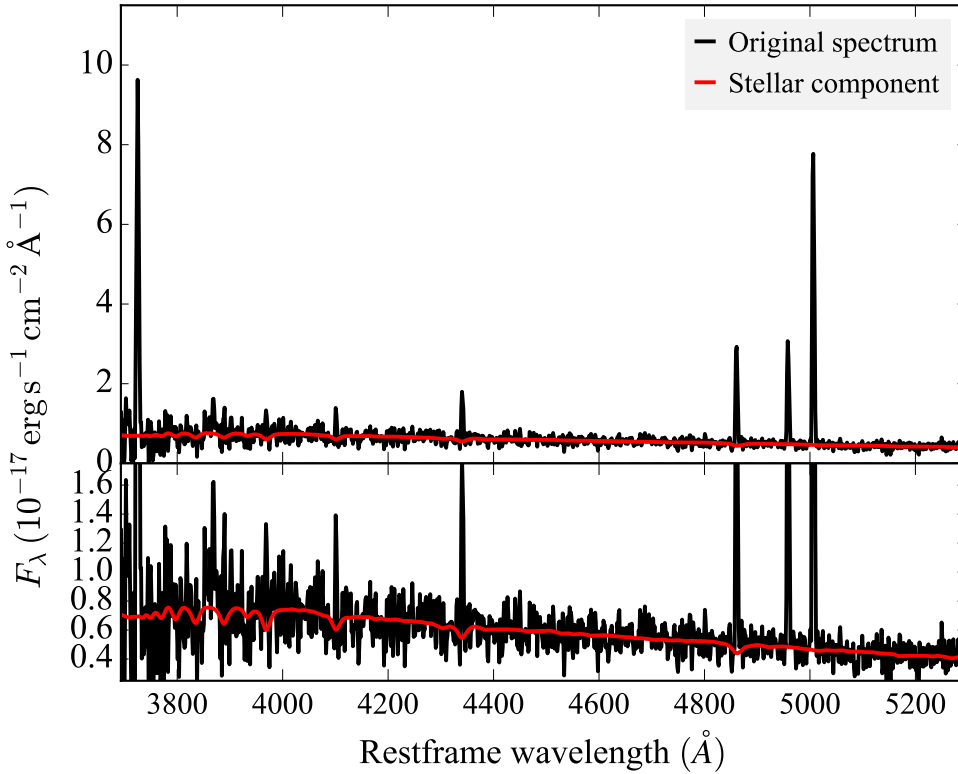

Fig. A.2: FORS2 600*B* spectrum of the explosion site i.e., the SN region. **Black is the original spectrum and red represents the fitted stellar component. The *upper panel* shows the full flux range, while the *lower panel* is a zoom in to the stellar continuum.**

In particular the $600B$ spectra (Figs. A.1 and A.2) are taken under excellent atmospheric conditions leading to a width of the spectral line spread function of FWHM=0″.6 at 5000 Å as evidenced by the trace of a bright stellar source serendipitously on the slit at a distance of 22″.0 to the WR region (seen at RA(J2000) = $19^h35^m02^s.00$, Decl(J2000) = $-52°50'21''.1$ in Fig. 1). The $600RI$ data have somewhat worse spatial resolution (FWHM=1″.0 at 7000 Å). This mismatch leads to the complication that the two different spectra are convolved with very different spatial scales. Due to the small angular size of the of WR region core ($\lesssim$ 0″.1 via HST imaging), and the gradient in physical properties, ratios of lines observed in the two different setups (e.g. for a determination of the dust reddening) are thus clearly non-trivial to interpret.

Table A.1 contains line fluxes and equivalent widths from our analysis of the FORS2 spectra, sometimes significantly different to the original Hammer et al. (2006) values. Their actual error on the line fluxes remains unfortunately unclear, but a substantial uncertainty of at least 25% must be present (as estimated from the apparent discrepancy between their line-flux ratios of [O III](λ5007)/[O III](λ4959) and [N II](λ6584)/[N II](λ6548) to the theoretical value of 2.98 set by magnetic-dipole transition probabilities and observed in high-quality SDSS spectra (e.g. Storey & Zeippen 2000; Osterbrock & Ferland 2006; Wesson et al. 2016).

Table A.1: Emission line fluxes and EW measurements from FORS2/VLT long-slit spectra for the GRB 980425/SN 1998bw host galaxy

	SN region[a]		WR region[b]	
	Flux[c]	EW_{rest} (Å)	Flux[c]	EW_{rest} (Å)
[O II](λ3727)	47 ± 2	48 ± 3	41 ± 3	250 ± 5
[Ne III](λ3968)	4.3 ± 0.6	3.1 ± 0.9	8.2 ± 0.2	52 ± 2
Hδ	2.6 ± 0.5	3.6 ± 0.8	7.7 ± 0.2	51 ± 2
Hγ	5.6 ± 0.5	9.0 ± 1.2	14.7 ± 0.3	57 ± 3
[O III](λ4363)	0.6 ± 0.2	2.2 ± 0.8	1.54 ± 0.05	10 ± 1
Hβ	12.4 ± 1.1	24 ± 2	34.6 ± 1.4	313 ± 3
[O III](λ4959)	12.9 ± 1.2	24 ± 2	68 ± 2	650 ± 5
[O III](λ5007)	40 ± 2	75 ± 4	205 ± 4	1980 ± 20
[N II](λ6548)[b]	1.3 ± 0.2	5.0 ± 1.0	1.57 ± 0.03	25 ± 1
Hα	38.5 ± 1.6	115 ± 6	77 ± 2	1220 ± 20
[N II](λ6584)	4.9 ± 0.3	15.9 ± 1.8	4.7 ± 0.2	79 ± 3
[S II](λ6717)	7.8 ± 0.3	29 ± 2	4.4 ± 0.2	87 ± 3
[S II](λ6731)	5.9 ± 0.3	20 ± 2	3.4 ± 0.3	70 ± 3

Notes. [a] To increase the S/N ratio, we include the adjacent two pixels in the extraction for the SN region. [b] Derived from the spectrum at the peak of the emission of the WR region. [c] Fluxes are given as 10^{-16} erg s^1 cm^{-2}. [d] The double horizontal line separates the nebular lines that were taken in the two different FORS2 setups. Due to the different width of the line spread function and thus angular scales observed in both setups, the lines below and above the horizontal line cannot easily be used together to infer physical properties.

From the Hβ/Hγ and Hβ/Hδ ratio, we measure $E_{B-V} = 0.22 ± 0.03$ mag for the WR and $E_{B-V} = 0.08^{+0.23}_{-0.08}$ mag for the SN region, both perfectly consistent with the MUSE data[11]. Also other properties are very similar to our IFU-based values as given in Table 1.

Finally, we exploit the bluer response of the FORS2 $600B$ grism to obtain an age of the H II region through a fit using composite stellar templates in `starlight` in a similar manner as

---

[11]We would measure significant dust reddening if we would not correct our Hβ, Hγ, or Hδ fluxes for stellar Balmer absorption.
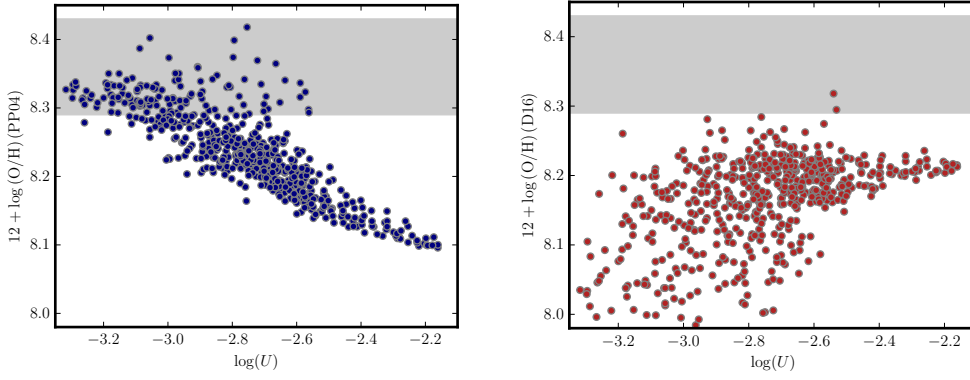
Fig. B.1: Dependence of the inferred oxygen abundance in two strong-line diagnostic ratios (*upper panel*: O3N2 from Pettini & Pagel 2004, *lower panel*: S2 from Dopita et al. 2016) on the ionization parameter U (using the [S III] to [S II] ratio) for the WR region. Each data point corresponds to a single spaxel, and the grey region indicates the metallicity constraints from the temperature-sensitive [O III](λ4363) emission line.

in the main text. The stellar population in the WR region is extremely young, and the Bruzual & Charlot (2003) template with an age of 1 Myr dominates the best fit by contributing ~60% to 90% to the total observed star light in various fits using different spectral templates and reddening laws. This very young age is consistent with the extremely high EW of [O III] and Hα (Table A.1), and the age constraints derived in the main text.

The SN region has prominent stellar components with ages of 5 Myr and 40 Myr (each contributing around 30% to the best-fit composite template), the younger of which is again consistent with the age estimate from the Hα EW in the main text.

Appendix B: Dependence of O3N2-based Oxygen Abundance on Ionization Parameter

To better illustrate how a changing ionization parameter U affects the metallicity measurement in the O3N2 or N2-scales we show U (defined as ionizing photons per hydrogen atoms) versus $12 + \log(\mathrm{O/H})$ in the Pettini & Pagel (2004) or Dopita et al. (2016) scale of the brightest H II-region in ESO184-G82 in Fig. B.1. Here, we use the [S II]/[S III] ratio (Fig. 6) to calculate U via photo-ionization models (Dors et al. 2011). Different parameterizations in U (e.g. Morisset et al. 2016) do not change Fig. B.1 significantly. The [S II]/[S III] ratio has the advantage of being nearly insensitive to metallicity, so we should not see a strong correlation between both quantities in accurate metallicity diagnostics. It is again clear, however, that the O3N2 metallicity scale only reproduces the H II-region metallicity in spaxels with lower ionization parameter, and systematically under-predicts it at higher U. In contrast, the Dopita et al. (2016) diagnostic is mostly independent on ionization parameter, but seems offset by an average ~0.15 dex towards lower $12 + \log(\mathrm{O/H})$ (Fig. B.1, lower panel).